

*Chapter***THE INNER CRUST AND ITS STRUCTURE**

***Débora P. Menezes⁽¹⁾, Sidney S. Avancini⁽¹⁾,
Constança Providência⁽²⁾ and Marcelo D. Alloy⁽³⁾ ****

⁽¹⁾ Depto de Física - Universidade Federal de Santa Catarina,
CP 476 - CEP 88040-900, Florianópolis, SC, Brazil

⁽²⁾ Centro de Física Computacional, Departamento de Física,
Universidade de Coimbra, 3004-516 Coimbra, Portugal

⁽³⁾ Universidade Federal da Fronteira Sul,
Chapecó, SC, CEP 89.812-000, Brazil

Abstract

In this chapter we discuss some possible physical pictures that describe the constitution of the inner crust of compact objects. Different relativistic models both with constant couplings and density dependent ones are used. We calculate the liquid-gas phase transition in asymmetric nuclear matter from the thermodynamic and dynamic instabilities. The equations of state used to describe the crust are related to the crust-core transition properties. Cold and warm pasta phases with and without alpha particles are constructed. The influence of the pasta phase and its internal structure on the diffusion coefficients associated with Boltzman transport equations used to simulate the evolution of protoneutron stars are shown. Finally, the possible existence of bare quark stars and the effects of strong magnetic fields on quark matter are considered. Open questions are pointed out.

*E-mail debora@fsc.ufsc.br

PACS 05.45-a, 52.35.Mw, 96.50.Fm.

Keywords: phase transitions, pasta phase, quark stars

1. Introduction

The internal constituents of compact stars are a great source of speculation [1]. They could be made of hadronic matter only, quark matter only (a possibility arisen by the Bodmer-Witten conjecture [2, 3]), or they could be hybrid. Hybrid stars may have in their interior hadrons and quarks with or without a condensate. If the star is composed of quark matter only, it may be a bare star and we will tackle this point at the end of this chapter. On the other hand, if it is made of hadrons only or if it is a hybrid object, it has a crust, our main interest in what follows. The crust mass and thickness depend on the equation of state (EOS) that describes the star. They also depend on the total stellar mass; an increase of the stellar mass increases the gravitational pull within the crust resulting in the thinning of the crust. An estimation of the size of the crust done in [5] gives values varying from 1.01 to 0.29 Km. In particular, we will discuss the possible existence of inhomogeneous structures, i. e. the pasta phase, in the inner crust due to the competition between the strong and Coulomb interactions and their implications for the properties of the crust.

Through out this chapter, we consider a system of protons and neutrons with mass M interacting with and through an isoscalar-scalar field ϕ with mass m_s , an isoscalar-vector field V^μ with mass m_v , an isovector-vector field \mathbf{b}^μ with mass m_ρ . We also include a system of leptons composed by electrons and muons, electrons and neutrinos or just electrons, depending on the problem. The Lagrangian density reads:

$$\mathcal{L} = \sum_{i=p,n} \mathcal{L}_i + \mathcal{L}_\sigma + \mathcal{L}_\omega + \mathcal{L}_\rho + \mathcal{L}_\gamma + \sum_{l=e,\nu,\mu} \mathcal{L}_l, \quad (1)$$

where the nucleon Lagrangian density has the form

$$\mathcal{L}_i = \bar{\psi}_i [\gamma_\mu iD^\mu - M^*] \psi_i, \quad (2)$$

with

$$iD^\mu = i\partial^\mu - \Gamma_v V^\mu - \frac{\Gamma_\rho}{2} \vec{\tau} \cdot \mathbf{b}^\mu - e \frac{1 + \tau_3}{2} A^\mu, \quad (3)$$

$$M^* = M - \Gamma_s \phi. \quad (4)$$

The lepton Lagrangian density is given by

$$\mathcal{L}_l = \bar{\psi}_l [\gamma_\mu (i\partial^\mu + eA^\mu) - m_l] \psi_l, \quad (5)$$

where e , m_l stand for the charge and mass of the lepton, respectively, and the meson Lagrangian densities are

$$\begin{aligned} \mathcal{L}_\sigma &= \frac{1}{2} \left(\partial_\mu \phi \partial^\mu \phi - m_s^2 \phi^2 - \frac{1}{3!} \kappa \phi^3 - \frac{1}{4!} \lambda \phi^4 \right), \\ \mathcal{L}_\omega &= \frac{1}{2} \left(-\frac{1}{2} \Omega_{\mu\nu} \Omega^{\mu\nu} + m_v^2 V_\mu V^\mu \right), \\ \mathcal{L}_\rho &= \frac{1}{2} \left(-\frac{1}{2} \mathbf{B}_{\mu\nu} \cdot \mathbf{B}^{\mu\nu} + m_\rho^2 \mathbf{b}_\mu \cdot \mathbf{b}^\mu \right), \\ \mathcal{L}_\gamma &= -\frac{1}{4} F_{\mu\nu} F^{\mu\nu}, \end{aligned}$$

where $\Omega_{\mu\nu} = \partial_\mu V_\nu - \partial_\nu V_\mu$, $\mathbf{B}_{\mu\nu} = \partial_\mu \mathbf{b}_\nu - \partial_\nu \mathbf{b}_\mu - \Gamma_\rho (\mathbf{b}_\mu \times \mathbf{b}_\nu)$ and $F_{\mu\nu} = \partial_\mu A_\nu - \partial_\nu A_\mu$. The parameters of the models are the nucleon mass $M = 939$ MeV, the coupling parameters Γ_s , Γ_v , Γ_ρ of the mesons to the nucleons, the electron mass $m_e = 0.511$ MeV, the muon mass $m_\mu = 105.66$ MeV and the electromagnetic coupling constant $e = \sqrt{4\pi/137}$. The electron neutrino mass is considered to be zero. In the above Lagrangian density $\vec{\tau}$ are the Pauli matrices. When density dependent models are used, the non-linear terms are not present and, hence, $\kappa = \lambda = 0$ and the density dependent parameters are chosen as in [4, 6, 7]. For the parametrizations with constant couplings, Γ_i is replaced by g_i , where $i = s, v, \rho$ as in the NL3 parameter set [8].

Some expressions are often used next. Y_p and Y_L refer to the proton and lepton fractions respectively. If matter in β -equilibrium is considered in a system of protons, neutrons, electrons and possibly trapped electron neutrinos, one has:

$$\mu_p = \mu_n - (\mu_e - \mu_\nu). \quad (6)$$

For neutrino free matter $\mu_\nu = 0$. Neutrality of charge requires $\rho_p = \rho_e + \rho_\mu$ and, if ρ_μ is present, its chemical potential is equal to the electron chemical potential.

2. Instabilities in Nuclear Matter

It was shown in [9, 10] that the pressure and density at the inner boundary of the crust (transition pressure and transition density) define the mass and moment

of inertia of the crust. This establishes a relation between the equation of state (EOS) and compact-star observables. In this section we show how an estimation of the transition properties may be obtained from the thermodynamical binodal and spinodal surfaces, or the dynamical spinodal. A better estimation, obtained from the pasta phase calculation, will be discussed in section 3.

The liquid-gas phase transition at subsaturation densities is a well known feature of the nuclear EOS [11]. It corresponds to the presence of a negative curvature of the free energy density \mathcal{F} . In this case the system is unstable against separation into two infinite homogeneous phases. The spinodal surface, which limits the unstable region in the (T, ρ_p, ρ_n) space, is defined by the cancellation of the determinant of the free energy curvature matrix [12]:

$$C_{ij} = \left(\frac{\partial^2 \mathcal{F}}{\partial \rho_i \partial \rho_j} \right)_T, \quad \mathcal{C} = \begin{pmatrix} \frac{\partial \mu_n}{\partial \rho_n} & \frac{\partial \mu_n}{\partial \rho_p} \\ \frac{\partial \mu_p}{\partial \rho_n} & \frac{\partial \mu_p}{\partial \rho_p} \end{pmatrix}.$$

The eigenvalues of the curvature matrix are given by

$$\lambda_{\pm} = \frac{1}{2} \left(\text{Tr}(\mathcal{C}) \pm \sqrt{\text{Tr}(\mathcal{C})^2 - 4\text{Det}(\mathcal{C})} \right),$$

and are associated to the eigenvectors $\delta \rho_{\pm}$. Inside the spinodal region the lowest eigenvalue λ_- is negative. The direction of the vector $\delta \rho_-$ defines the direction of instability, which generally dictates a distillation effect corresponding to a phase separation into a high density symmetric matter and low density neutron rich matter [12].

In the left panel of Fig.1 the spinodal sections obtained for different relativistic mean field (RMF) models are plotted in terms of the total density ρ and the asymmetry parameter

$$\delta = (\rho_n - \rho_p)/\rho = 1 - 2Y_p. \quad (7)$$

While for symmetric matter most of the models show a similar behavior, at high asymmetry and/or temperature models differ. For this reason, establishing constraints on the equations of state based on experimental results is an important step, and a discussion on this aspect is done in section 4. In the right panel of Fig. 1, the spinodal sections for several temperatures and two models (NL3 [8] and TW [4]) are an example of the possible existing differences: for TW with a symmetry energy and corresponding slope equal, respectively, to 32.76 and 55.30 MeV, the transition density (identified by a full dot) occurs at a larger

density and for a smaller proton fraction than for NL3 with a symmetry energy and slope equal, respectively, to 37.34 and 118.30 MeV. Also, for TW the spinodal surface extends to a larger temperature.

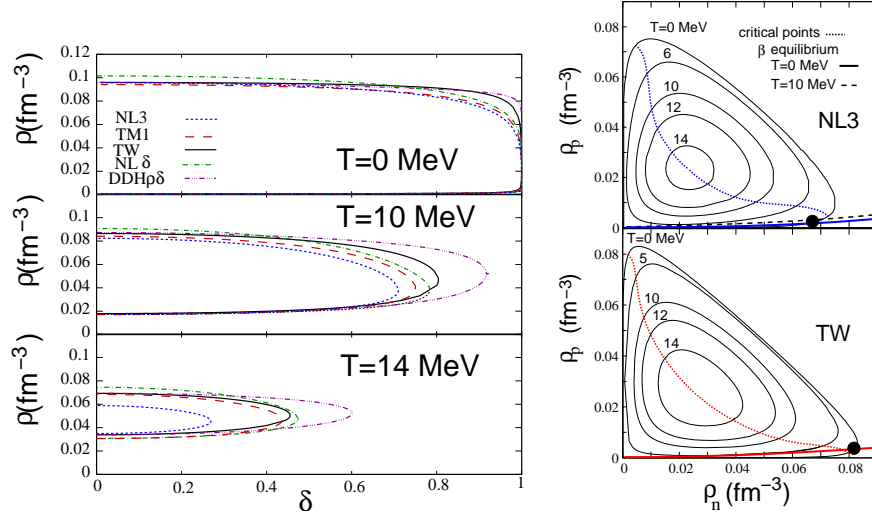


Figure 1. Left panel: the spinodal section for different RMF models in the $\rho - \delta$ plane. Fig. taken from [7]. Right panel: the spinodal section for NL3 and TW and different temperatures. The β -equilibrium EOS at $T = 0$ ($T = 10$) MeV is represented by a full (dashed) line. The full dot identifies the transition crust-core at $T = 0$. Fig. taken from [12].

Instead of using a thermodynamic approach, in [13] the transition density was estimated in a local equilibrium approximation by calculating the density for which matter becomes unstable to small density fluctuations. An equivalent approach is the Vlasov formalism, a semi-classical limit of the description of the collisionless regime, which has been used in [14] to calculate the dynamical spinodal within several RMF models. Contrary to the calculation of the thermodynamical spinodal, the effect of the finite range of the nuclear interaction as well as the Coulomb interaction and the presence of electrons is taken into account in the determination of the dynamical spinodal.

In the Vlasov formalism the equilibrium state, characterized by the Fermi momenta of neutrons, protons and electrons, p_{Fn} , p_{Fp} , p_{Fe} , is the starting point. Charge neutrality requires $p_{Fe} = p_{Fp}$. A perturbation of the system

is then described by the perturbed mesonic fields, $F_i = F_{i0} + \delta F_i$, and the perturbed distribution functions for the neutrons, protons and electrons

$$f_i(t, \mathbf{r}, \mathbf{p}) = f_{0i} + \delta f_i, \quad \delta f_i = \{S_i, f_{0i}\},$$

where $f_{0i} = \theta(p_{F_i}^2 - p^2)$ and the generating function $S(\mathbf{r}, \mathbf{p}, t) = \text{diag}(S_p, S_n, S_e)$ has been introduced. The time evolution of the distribution function f_i is described by the Vlasov equation [14]

$$\frac{\partial f_i}{\partial t} + \{f_i, h_i\} = 0, \quad i = p, n, e.$$

In the limit of small perturbations the linearized Vlasov equation

$$\frac{dS_i}{dt} + \{S_i, h_{0i}\} = \delta h_i$$

is solved. In this equation h_{0i} and δh_i stand, respectively, for the equilibrium single particle Hamiltonian and corresponding perturbation from equilibrium, and $\{v, w\}$ represents the Poisson bracket of two dynamical functions v and w . Longitudinal fluctuations are described by the ansatz

$$\begin{pmatrix} S_i & \delta F_j & \delta \rho_i & \delta h_i \end{pmatrix} = \begin{pmatrix} S_{\omega,i}(x) & \delta F_{\omega,j} & \delta \rho_{\omega,i} & \delta h_{\omega,i} \end{pmatrix} e^{i(\mathbf{q} \cdot \mathbf{r} - \omega t)},$$

where \mathbf{q} and ω are the transferred momentum and energy and $x = \cos(\mathbf{p} \cdot \mathbf{q})$. The dynamical spinodal surface is characterized by a zero frequency ω .

It is expected that the transition density lies in the metastable region between the binodal surface and the dynamical spinodal surface. The binodal surface is defined in the ρ, Y_p, T phase space as the surface where the gas and liquid phases coexist, and it defines an upper limit for the extension of the pasta phase since it also does not take into account Coulomb nor finite size effects. The binodal surface is calculated imposing Gibbs conditions: for a given temperature, the pressure and the proton and neutron chemical potentials are equal in both phases [11]. The thermodynamical spinodal touches the binodal surface at the critical point, which, for a given temperature, occurs for the largest pressure on both surfaces and at a density and proton fraction close to the crust-core transition density and proton fraction of cold stellar β -equilibrium matter. This is represented in Fig. 2a) where the square and the circle represent respectively the crust-core transition from the thermodynamical spinodal and binodal. Both the EOS of β -equilibrium neutrino free matter and matter with trapped neutrinos are represented. We conclude that for neutrino free matter both estimations

almost coincide, while for matter with a lepton fraction $Y_L=0.4$ there is a large difference. As stated before, it is possible to get a better estimation of the lower limit of the pasta phase extension if, instead of the thermodynamical spinodal, the dynamical spinodal is calculated, as in Fig. 2b). Taking into account finite range effects and electrons makes the spinodal region smaller, so even though the thermodynamical method gives a good estimation of the transition density for cold β -equilibrium matter, it is a bit too large. This is confirmed by pasta calculations [16] as seen in the next section.

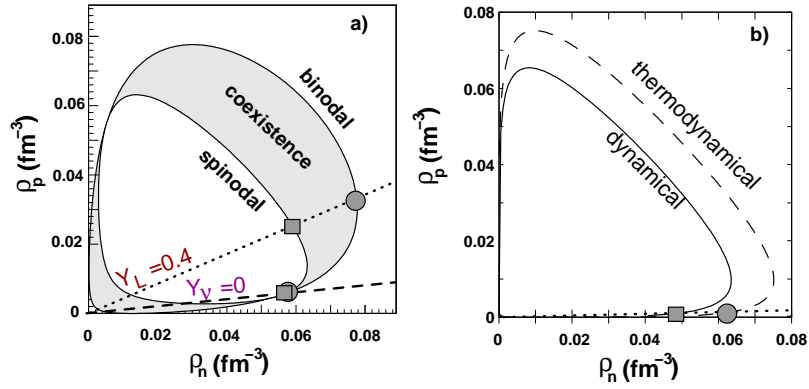


Figure 2. The transition density for neutrino free β -equilibrium matter and matter with trapped neutrinos and a fraction of leptons $Y_L = 0.4$: a) estimation from the spinodal and binodal sections; b) estimation from the dynamical and thermodynamical spinodal.

For densities inside the dynamical spinodal matter is non-homogeneous, and for densities outside the binodal surface, matter is homogeneous. Between these two surfaces we may find matter in a metastable configuration. The most probable configuration is the one with the smallest free energy density and requires a pasta phase calculation, the topic of the next section.

3. Cold and Warm Pasta Phase

In the inner crust of a neutron star (NS), a liquid gas phase transition can give rise to the existence of the pasta phase, which is a frustrated system that arises from the competition between the strong and the electromagnetic interactions.

The pasta phase appears at densities on the order of $0.001 - 0.1 \text{ fm}^{-3}$ in neutral nuclear matter and at a smaller density range in β -equilibrium stellar matter. The basic shapes of these structures were named as droplets (bubbles), rods (tubes) and slabs for three, two and one dimensions respectively. The ground-state configuration is the one that minimizes the free energy. In what follows we use two different prescriptions in order to build the pasta phase at zero and finite temperatures: one is based on phase coexistence (CP) and obeys the Gibbs conditions, and the other is the Thomas-Fermi (TF) approximation. Within the CP method, the pasta structures are built with different geometrical forms in a background nucleon gas. This is achieved by calculating from the Gibbs' conditions the density and the proton fraction of the pasta and of the background gas, so that in the whole we have to solve simultaneously various equations. These equations are related to the fact that the pressure, proton and neutron chemical potentials and temperature are the same in both phases. Two more equations are related to the nucleon effective mass in each phase, and an equation that balances the amount of protons in each phase has also to be solved:

$$f(\rho_p^I) + (1 - f)(\rho_p^{II}) = Y_p \rho, \quad (8)$$

where I and II label each of the phases, f is the volume fraction of phase I:

$$f = \frac{\rho - \rho^{II}}{\rho^I - \rho^{II}}, \quad (9)$$

where the total baryonic density is

$$\rho = \rho_p + \rho_n, \quad (10)$$

and Y_p is the global proton fraction.

The correct parametrization of the surface energy, which is temperature, proton fraction and geometry dependent, must be used [17]. The following functional for the surface tension coefficient, σ , is used,

$$\sigma = \sigma(x, T = 0) [1 - a(T) xT - b(T)T^2], \quad (11)$$

where $x = \delta^2$ stands for the square of the asymmetry parameter defined in eq.(7). The CP method is very easy to implement; however, since it is not self-consistent, the results obtained within the method should be taken with care. The self-consistent Thomas Fermi results should be compared with other more

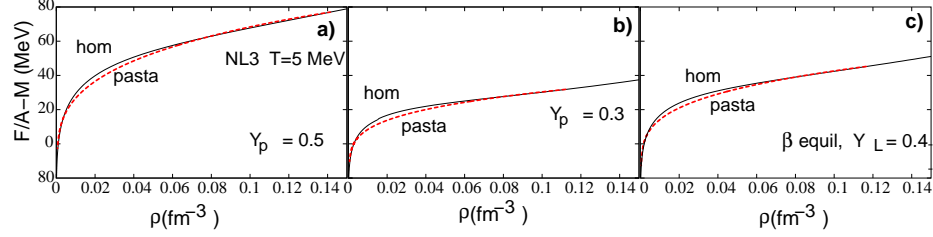


Figure 3. Free energy for the homogeneous and pasta like matter. The red dashed line defines the pasta free energy. The crossing of the pasta and the homogeneous free energy define the extension of the pasta phase.

realistic, yet more involving methods that do not impose a pre-defined form, such as the quantum molecular dynamics calculation in [18] or the 3D Skyrme-Hartree-Fock method at finite temperature used in [19].

In Fig. 3 we plot the free energy per particle for homogeneous and pasta like matter described by the NL3 model within CP, with $T=5$ MeV and proton fractions $Y_p = 0.5, 0.3$ and for β -equilibrium matter with trapped neutrinos for a lepton fraction $Y_L = 0.4$. This figure illustrates well the effect of the pasta phase on the free energy: the formation of a non-homogeneous phase is energetically favored. The system in equilibrium chooses the configuration with the lowest free energy, so the pasta-like matter defines the ground state of the system if its free energy is lower than the free energy of the corresponding homogeneous matter. The upper density limit of the pasta phase lies inside the binodal surface and decreases when the proton fraction decreases. For β -equilibrium matter this limit defines the NS crust-core transition.

In Fig. 4 we compare the estimations for transition density from a non-homogeneous phase to a homogeneous phase obtained from the binodal surface (Bin) [11], the dynamical spinodal surface (Sp-d) [13, 14] the thermodynamic spinodal surface (Sp-t) [12] and from the CP and TF methods. The TF results lie always between the results obtained from the dynamical spinodal and the binodal surfaces. This is a self-consistent method that should satisfy these two constraints. The CP calculation may predict results at densities that lie below the dynamical spinodal value, namely at high temperatures and symmetric matter. For CP to give reasonable results, it is important that a good parametrization of the surface energy is used. The thermodynamical-spinodal calculation always

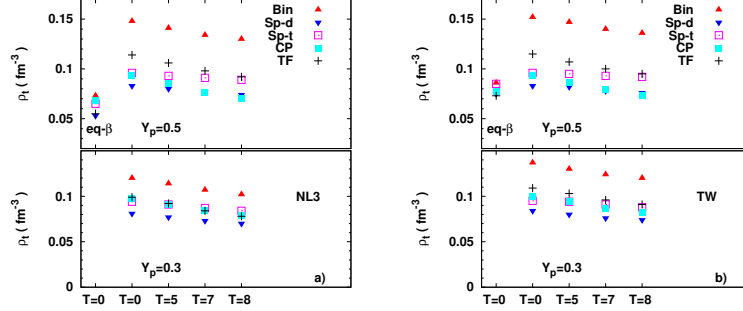


Figure 4. Transition density, for several temperatures and proton fractions $Y_p = 0.5$ (upper plots), 0.3 (lower plots) and β -equilibrium (eq- β) at $T=0$ (left part of upper plots), obtained using different methods within the models a) NL3 and b) TW. Fig. taken from [15].

gives a quite good estimation even though it does not take into account neither the surface nor the Coulomb effects. For β -equilibrium matter all methods give similar results. This is due to the occurrence of the transition density close to the critical point where the spinodal and binodal surfaces touch and the pressure on these surfaces is maximum.

In Fig. 5 we compare the density range for which each pasta configuration exists within NL3 and TW. The thick lines stand for the Thomas-Fermi calculation, the thin ones for the CP method. Full lines represent TW and dashed ones NL3. For symmetric matter the main difference between the models is the appearance of the different phases at slightly smaller densities within NL3. However, the largest differences occur for $Y_p = 0.3$: NL3 has a much smaller rod phase and no slab phase at $T=7$ and 8 MeV and quite large tube and bubble phases. The figure also illustrates the power and limitations of the simpler method CP: the onset at lower densities of the pasta phase is quite well described, however, it fails to describe the bubble phase and predicts a smaller crust-core transition density.

It is important to point out that Figs. 4 and 5 are slightly different from the ones published in [16] for the cases $Y_p = 0.3$ and matter in β -equilibrium because a slightly different parameterization of the surface coefficient was used, i.e., in eq.(7), the proton fraction was taken as the proton fraction of the denser phase in [16] and here it was taken as the global proton fraction.

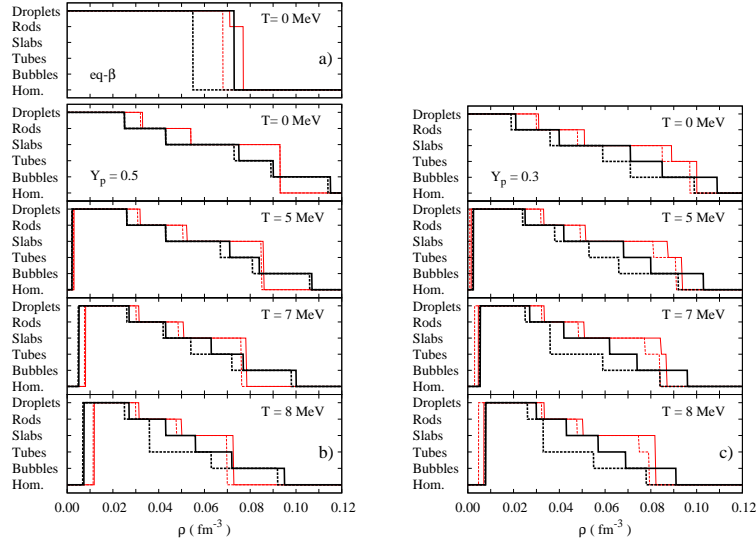


Figure 5. Pasta phases: comparison between NL3 (dashed line) and TW (full line) and the methods CP (thin red lines) and TF (thick lines) for a) β -equilibrium cold stellar matter; b) $Y_p = 0.5$, c) $Y_p = 0.3$. Fig. taken from [15].

The importance of the α particles cannot be neglected. It is the most strongly bound system among all light clusters and it certainly plays a role in nuclear matter, mainly at low temperatures. The Lagrangian density that describes the α particles can be added to Eq. 1 and is given by [20]:

$$\mathcal{L}_\alpha = \frac{1}{2}(iD_\alpha^\mu \phi_\alpha)^*(iD_{\mu\alpha} \phi_\alpha) - \frac{1}{2}\phi_\alpha^* M_\alpha^2 \phi_\alpha, \quad (12)$$

with $iD_\alpha^\mu = i\partial_\alpha^\mu - \Gamma_\alpha V^\mu$, where $M_\alpha = 4M - B_\alpha$, $B_\alpha = 28.3$ MeV.

The coupling of the ω meson to the α -particles is included for mimicking the excluded volume effect and, consequently, the α particles dissolution at high densities. The dissolution density obtained using the ansatz $\Gamma_\alpha = 4\Gamma_v$ is in agreement with the dissolution densities obtained within a quantum statistical approach [20]. More careful studies are necessary in order to determine the adequate meson-cluster couplings. When α particles are included, Eq.(8)

becomes

$$f(\rho_p^I + 2\rho_\alpha^I) + (1 - f)(\rho_p^{II} + 2\rho_\alpha^{II}) = Y_p \rho, \quad (13)$$

where I and II label each of the phases, f is the volume fraction of phase I given in eq.(9), where the total baryonic density is now

$$\rho = \rho_p + \rho_n + 4\rho_\alpha, \quad (14)$$

and Y_p is the global proton fraction given by

$$Y_p = \frac{\rho_p + 2\rho_\alpha}{\rho}. \quad (15)$$

The α particle densities are plotted in Fig. 6 for $Y_p = 0.5$ and 0.3 and $T = 5$ and 8 MeV. We include the calculation for both homogeneous matter and pasta-like matter. This figure gives a hint on the possible effects of α particles in the inner crust of a compact star, which is larger for the larger temperatures and larger proton fractions. Due to the existence of a non-homogeneous phase, the α -particles dissolve at larger densities, although the α fraction may take very small values. It is important to include other small clusters (deuteron, tritium and helium 3), which, due to their smaller masses will predominate over the α particles at the larger temperatures. We expect that the appearance of these light clusters will affect heat and transport properties.

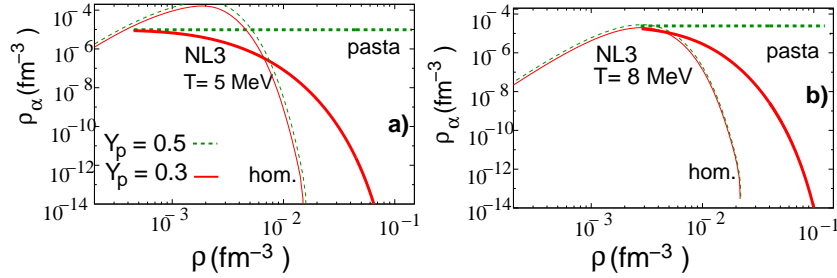


Figure 6. α particle density for a) $T=5$ MeV and b) $T=8$ MeV and $Y_p = 0.3$ and 0.5 obtained with NL3 for homogeneous matter (thin lines) and gas phase of the pasta-like matter (thick lines). Fig. taken from [17].

The properties of the pasta phase are also discussed in the chapter *Nuclear pasta in supernovae and neutron stars* by G. Watanabe and T. Maruyama, where different formalism and numerical methods are used.

4. Constraints on the Equations of State

We have seen that the EOS that describe equally well the properties of nuclear saturation matter and the ground-state properties of nuclei, predict quite different spinodal surfaces at high asymmetries and/or temperatures in Fig 1. The same occurs for other properties at high densities, such as the incompressibility.

The asymmetric nuclear matter EOS may be constrained by the properties of asymmetric nuclear matter obtained from various analyses of experimental data, including isospin diffusion measurements [21], giant resonances [22], isobaric analog states [23] or meson production (pions [24], kaons [25]) in heavy ion collisions (see [26] for an overview).

Some correlations between finite nuclei properties and bulk matter properties have been obtained: a linear relation between the density derivative of the neutron matter EOS at 0.1 fm^{-3} and the neutron skin thickness of ^{208}Pb that has been theoretically tested with different Skyrme parameter sets [27] and relativistic Hartree models [28]. Another linear correlation was obtained between the ^{208}Pb skin thickness and the liquid-to-solid transition density in neutron stars [29]. In what follows the neutron skin thickness is defined as

$$\delta R = R_n - R_p, \quad (16)$$

where the mean square radius is

$$R_i^2 = \frac{\int d^3r r^2 \rho_i(\mathbf{r})}{\int d^3r \rho_i(\mathbf{r})}. \quad i = p, n. \quad (17)$$

Accurate measurements of neutron skin thicknesses, via future parity violating experiments [30] or by means of existing antiprotonic atoms data [31, 32], are thus helpful in determining the bulk properties of nuclear systems.

The other important quantity, the slope of the symmetry energy, is given by

$$L = 3\rho_0 \frac{\partial \mathcal{E}_{sym}(\rho)}{\partial \rho} \Big|_{\rho=\rho_0}, \quad \mathcal{E}_{sym} = \frac{1}{2} \frac{\partial^2 \mathcal{E}/\rho}{\partial \delta^2} \Big|_{\delta=0}. \quad (18)$$

Using a wide range of effective nuclear models, both phenomenological such as the non-relativistic Skyrme forces or RMF models and microscopic Brueckner-Hartree Fock with the realistic AV18 potential plus a three-body force of the Urbana type [33], we have confirmed the existence of a linear correlation between the symmetry energy slope L and the crust-core transition density obtained from the thermodynamical spinodal, see Fig. 7a). The same models predict a linear correlation between the neutron skin thickness of the ^{208}Pb

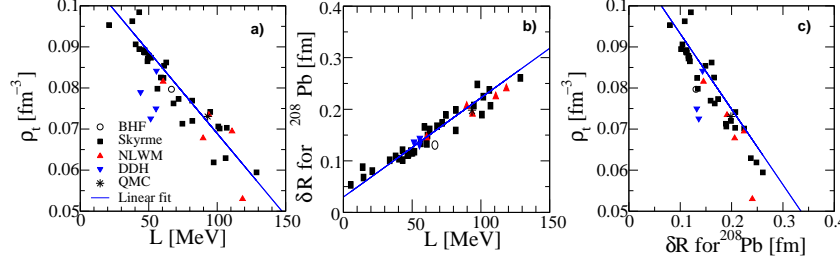


Figure 7. Correlations between a) the symmetry energy slope L and the transition density obtained from the thermodynamical spinodal; b) the symmetry energy slope L and the neutron skin thickness for ^{208}Pb ; c) the neutron skin thickness for ^{208}Pb and the transition density. Fig. taken from [33].

and L and, consequently, a correlation between the neutron skin thickness of the ^{208}Pb and the transition density ρ_t , as proposed in [29]. However, in [34] it was shown that no similar correlation exists between the transition pressure and the slope L , Fig. 8, due to the large dispersion of the predicted transition pressure obtained when independent models are considered. This means that an experimental determination of L alone is not enough for a good estimation of the crust mass and moment of inertia of a compact star, since it is the transition pressure that allows a prediction of the EOS from the observation of glitches [10].

5. Diffusion Coefficients and the Pasta Phase

The neutrino signals detected by astronomers can be used as a constraint to infer protoneutron star (PNS) composition. For the same purpose, theoretical studies involving different possible equations of state obtained for all sorts of matter composition have to be done because the temporal evolution of the PNS in the so-called Kelvin-Helmholtz epoch, during which the remnant compact object changes from a hot and lepton-rich PNS to a cold and deleptonized neutron star depends on two key ingredients: the equation of state (EOS) and its associated neutrino opacity [35]. All contributions from neutrino opacities are related with the diffusion coefficients and can be used as input to the solution of the transport equations in the equilibrium diffusion approximation to simulate the

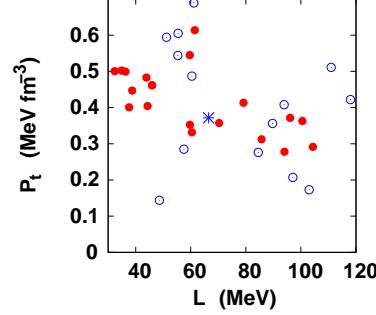


Figure 8. Transition pressure obtained from the thermodynamical spinodal as a function of the symmetry energy slope L for several Skyrme models (full dots), RMF models (empty dots) and a Brueckner-Hartree-Fock calculation [34].

Kelvin-Helmholtz phase of the protoneutron stars.

The diffusion coefficients that are related to the neutrino opacities are calculated in such a way that the formation of nuclear pasta at low densities is taken into account. The diffusion coefficients are given by [35]

$$D_k = \int_0^\infty d\epsilon_\nu \epsilon_\nu^k \lambda_\nu(\epsilon_\nu) f_\nu(\epsilon_\nu) (1 - f_\nu(\epsilon_\nu)), \quad k = 2, 3, 4, \quad (19)$$

where $\lambda_\nu(\epsilon_\nu)$ is the total mean free path of neutrinos and $f_\nu(\epsilon_\nu)$ is the Fermi-Dirac distribution.

To calculate neutrino opacities and mean free paths we consider neutral current scattering reactions $\nu_e + n \rightarrow \nu_e + n$ and $\nu_e + p \rightarrow \nu_e + p$ and charged current absorption reactions $\nu_e + n \rightarrow e^- + p$ and $\bar{\nu}_e + p \rightarrow e^+ + n$. Basically, it consists in calculating the cross sections $\sigma_{n,p}$ for neutrino-nucleon scattering reactions and the cross section σ_a for neutrino absorption reactions for both nondegenerate and degenerate thermodynamic limits as done in [36]. The thermodynamic regions of intermediate degeneracy are handled by a simple interpolation. The mean free path is given by $\lambda_\nu(\epsilon_\nu) = \frac{1}{\rho_n \sigma_n + \rho_p \sigma_p + \rho \sigma_a}$, where $\rho = \rho_p + \rho_n$ and they are related to the diffusion coefficients by

$$\lambda_\nu^k = \frac{D_k}{\int_0^\infty d\epsilon_\nu \epsilon_\nu^k f_\nu(\epsilon_\nu) (1 - f_\nu(\epsilon_\nu))}. \quad (20)$$

The diffusion coefficients D_2 , D_3 and D_4 are strongly dependent on the EOS and are functions of three thermodynamic variables: ρ , T and Y_L . We

start by fixing ρ , T and Y_L from the EOS to calculate the cross sections σ_p , σ_n and σ_a as function of the neutrino energy and then we integrate in neutrino energy. The numerical procedure used to calculate the diffusion coefficients to homogeneous and inhomogeneous matter is the same, except for the nucleon effective mass. The pasta structure is obtained by the coexistence phases method, which is based on the enforcement of the Gibbs conditions. Hence, all other thermodynamic variables (chemical potentials of all particle species, temperature, pressure and lepton fraction), necessary to calculate the neutrino mean free path, and consequently the diffusion coefficients of the pasta phase are equal in both phases. The nucleon effective mass, on the other hand, is not the same. To calculate $\lambda_\nu(\epsilon_\nu)$ we need the nucleon effective mass M^* . In the pasta phase, two different phases coexist (phase I and phase II). In our calculation, we have used $M^* = fM^{*(I)} + (1 - f)M^{*(II)}$ for the pasta phase.

Our results for the diffusion coefficients as a function of the baryon density at temperature $T = 5$ MeV and lepton fraction $Y_L = 0.4$ (includes electrons and trapped neutrinos) is shown in Fig. 9, from where we can see that only three structures are found inside the pasta phase for the present model: droplets, rods and slabs. While the diffusion coefficients obtained with homogeneous matter is always smooth and continuous, a common trend of all the diffusion coefficients obtained with the pasta phase is a kink at very low densities in between 0.01 and 0.015 fm^{-3} due to the fact that the effective nucleon mass becomes greater than the corresponding chemical potential.

In obtaining the diffusion coefficients, the EOS was calculated as a grid where temperature ranges are in between 0 and 50 MeV and densities vary from 0.005 to 0.5 fm^{-3} . We have calculated the diffusion coefficients only for baryonic densities above 0.005 fm^{-3} because the integrals of type (19) are very difficult to converge at lower densities. In all cases the diffusion coefficients obtained with homogeneous matter join the curves obtained with the pasta phase at densities higher than the ones shown in Fig 9. For D_2 calculated at $T=5$ MeV and $Y_L = 0.4$, for instance, they cross each other at $\rho = 0.12 \text{ fm}^{-3}$. Our codes interrupt the calculation once homogeneous matter becomes the ground state configuration. This means that there is always a gap in the diffusion coefficients when the transport equations are calculated with the inclusion of the pasta phase.

While the diffusion coefficients obtained with homogeneous matter are always smooth and continuous, a common trend of all the diffusion coefficients obtained with the pasta phase is a kink at very low densities in between 0.01

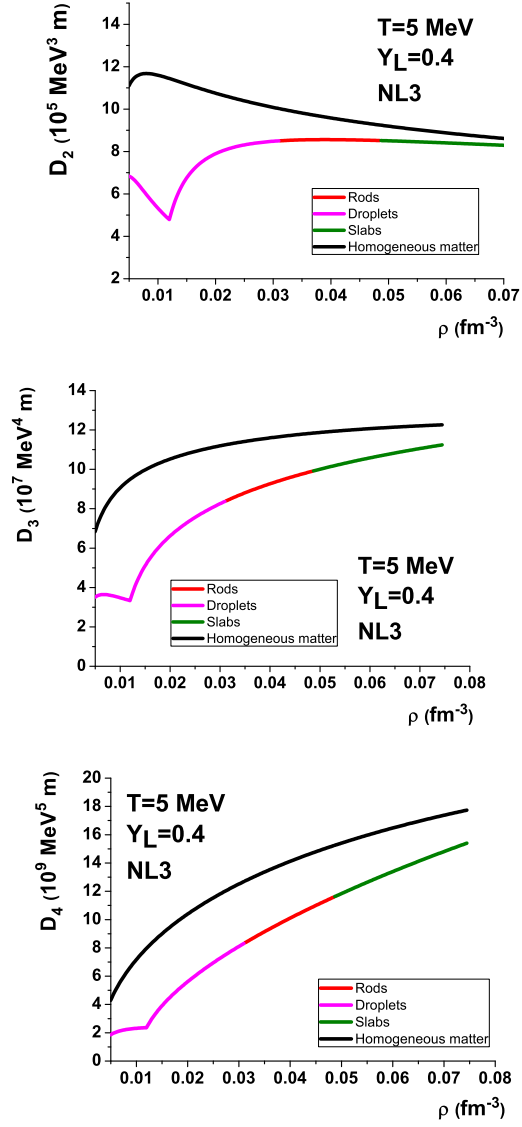


Figure 9. Diffusion coefficients D_2 , D_3 and D_4 as function of baryon density at $T = 5 \text{ MeV}$ and $Y_L = 0.4$ for homogeneous matter and pasta phase. Fig. taken from [37].

and 0.015 fm^{-3} . The interpolation procedure we use depends on the quantities $\eta_i = (\mu_i - M^*)/T$, $i = p, n$. Whenever either η_p or η_n inverts its sign, these kinks appear, i.e., they are the result of the effective nucleon mass being greater than the corresponding chemical potential. Moreover, the pasta phase diffusion coefficients are always lower than the corresponding coefficients obtained with homogeneous matter.

Our results show that the mean free paths are significantly altered by the presence of nuclear pasta in stellar matter when compared with the results obtained with homogeneous matter. These differences in neutrino opacities will have consequences in the calculation of the Kelvin-Helmholtz phase of protoneutron stars [37].

6. Quark Stars Subject to Strong Magnetic Fields

Neutron stars with very strong magnetic fields of the order of $10^{14} - 10^{15} \text{ G}$ are known as magnetars and they are believed to be the sources of the intense gamma and X rays detected in 1979 [38, 39]. The hypothesis that some neutron stars are constituted by unbound quark matter cannot be completely ruled out since the Bodmer-Witten conjecture [2] cannot be tested in earthly experiments. This conjecture implies that the true ground state of all matter is (unbound) quark matter because theoretical predictions show that its energy per baryon at zero pressure is lower than ^{56}Fe binding energy. According to [3] the quarks are bound by the strong force rather than the gravitational force that binds other stars. At the surface of the star, where the quark density drops abruptly to zero, the electrons extend into a layer of thickness of the order of 10^3 fm above the surface, where there is a super-strong electric field that ties the electrons to the star. If such a star would be covered by a crust of ordinary nuclear matter (and neutralizing electrons), it would be blown away as it forms [40] or would be destroyed by thermal effects [41]. Thus, one expects quark stars to be bare, in the sense that the surface is this thin layer of electrons [42].

We investigate quark matter described by the Nambu-Jona-Lasinio [43] model exposed to strong magnetic fields. In the case of pure quark matter, as predicted by the QCD phase transition possibly taking place in heavy ion collisions, the ultra-strong magnetic field results from the superposition of external and internal fields, the former generated by the alignment of charged particles that are spinning very rapidly. We use an external field to mimic the real situation.

In order to consider (three flavor) quark matter subject to strong magnetic fields we introduce the following Lagrangian density

$$\mathcal{L} = \mathcal{L}_f - \frac{1}{4} F_{\mu\nu} F^{\mu\nu} \quad (21)$$

where the quark sector is described by the $su(3)$ version of the Nambu–Jona-Lasinio model which includes scalar-pseudoscalar and the t’Hooft six fermion interaction that models the axial $U(1)_A$ symmetry breaking:

$$\mathcal{L}_f = \bar{\psi}_f [\gamma_\mu (i\partial^\mu - q_f A^\mu) - \hat{m}_c] \psi_f + \mathcal{L}_{sym} + \mathcal{L}_{det}, \quad (22)$$

where \mathcal{L}_{sym} and \mathcal{L}_{det} are given by:

$$\mathcal{L}_{sym} = G \sum_{a=0}^8 [(\bar{\psi}_f \lambda_a \psi_f)^2 + (\bar{\psi}_f i\gamma_5 \lambda_a \psi_f)^2], \quad (23)$$

$$\mathcal{L}_{det} = -K \{ \det_f [\bar{\psi}_f (1 + \gamma_5) \psi_f] + \det_f [\bar{\psi}_f (1 - \gamma_5) \psi_f] \}, \quad (24)$$

where $\psi_f = (u, d, s)^T$ represents a quark field with three flavors, $\hat{m}_c = \text{diag}_f(m_u, m_d, m_s)$ is the corresponding (current) mass matrix while q_f represents the quark electric charge, $\lambda_0 = \sqrt{2/3}I$ where I is the unit matrix in the three flavor space, and $0 < \lambda_a \leq 8$ denote the Gell-Mann matrices. Here, we consider $m_u = m_d \neq m_s$. A_μ and $F_{\mu\nu} = \partial_\mu A_\nu - \partial_\nu A_\mu$ are used to account for the external magnetic field. Since we are interested in a static and constant magnetic field in the z direction, $A_\mu = \delta_{\mu 2} x_1 B$. Whenever β -equilibrium neutrino-free matter is considered, the leptonic sector is given by eq.(5), where neutrinos are not taken into account. Besides the $su(3)$ version of the model, we also present two flavor $su(2)$ NJL model results for comparison.

In Fig. 10a) one can see that the inclusion of the magnetic field makes matter more and more bound in both versions of the model. For the present set of parameters, the energy per baryon E/A of magnetized quark matter becomes more bound than nuclear matter made of iron nuclei, $\frac{E}{A}|_{56Fe} \sim 930$ MeV for B around 2×10^{19} G.

The EOS for stellar matter under a strong magnetic field is obtained with a density dependent frozen magnetic field which is set equal to 10^{15} G at the surface and does not exceed 6×10^{18} G in the center of the star. Approximate values of the mass and radius of the stars obtained from the integration of the TOV equations [45] are displayed in Fig. 10b), from where it is seen that the

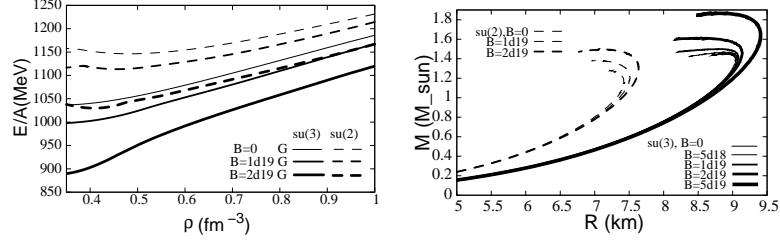


Figure 10. a) Energy per nucleon as a function of density for $B = 0, 10^{19}$ and 2×10^{19} G within NJL $su(2)$ and NJL $su(3)$; b) Mass-radius curves for the families of stars within NJL $su(2)$ and NJL $su(3)$. For $B \leq 10^{18}$ the curves coincide with the $B = 0$ results. Fig. taken from [44].

gravitational mass increases with the increase of the magnetic field for an intensity larger than $\sim 5 \times 10^{18}$ G for the $su(3)$ version and 10^{18} G for the $su(2)$ NJL. Another important effect of the field on the properties of the stars is the increase of the radius of the star. The largest radius may be as high as 9.5 Km for the $su(3)$ NJL. In general, the maximum mass star configurations for the $su(2)$ version of the NJL model are smaller with smaller radius, ~ 7 Km.

Next we discuss the effect of the magnetic field and temperature on quark matter as possibly formed in heavy-ion reactions. We display the free energy per particle in terms of the magnetic field for symmetric matter in Fig. 11a) and in terms of the density for asymmetric matter in Fig. 11b). As discussed before, the effect of the magnetic field is stronger for smaller densities and temperatures. At a given density the main effect of temperature is to decrease the free energy per particle. The effect of the magnetic field is clearly seen in Fig. 11a). It is stronger for the smaller temperatures and, for a strong enough field it gives rise to a decrease of the free energy (above $B = 4 \times 10^{18}$ G for $\rho = \rho_0$), due to a reduction of the number of Landau levels. However, for even stronger fields, the free energy increases due to an increase of the effective quark masses with B . This explains why in Fig. 11b) the free energy at $T=10$ MeV below $\rho = 0.5$ fm $^{-3}$ is smaller for $B = 2 \times 10^{19}$ G and larger for $B = 10^{20}$ G. For larger temperatures, the reduction observed at intermediate densities washes out and it is only observed an increase of the free energy for fields above 5×10^{19} G. The increase of the free energy for very large fields is mainly due to a reduction of the entropy and an increase of the effective mass for $B > 10^{19}$ G.

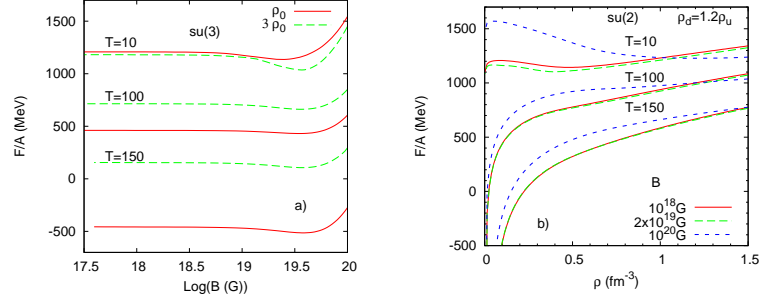


Figure 11. Free energy per particle for NJL a) $su(3)$ at $T = 10, 100, 150$ MeV as a function of B for symmetric quark matter and $\rho = \rho_0$ and $3\rho_0$; b) $su(2)$ versus the density for asymmetric matter $\rho_d = 1.2\rho_u$, $T = 10, 100, 150$ MeV and $B = 10^{18}, 2 \times 10^{19}, 10^{20}$ G. Fig. taken from [46]

To extend the present calculation in order to consider matter in protoneutron stars, the enforcement of charge neutrality and β -equilibrium is required. The ideal calculation would consider a fixed entropy resulting in temperatures lower than 50 MeV in the interior of the stars. This extension is simple and straightforward.

7. Conclusions and open questions

In this chapter we have focused on the study of possible internal structures of the neutron stars crust. The existence of the pasta phase is related to the instabilities and possible coexisting phases in the nuclear matter, features well described by the spinodal and binodal sections. Important remaining questions are: at which temperatures do the pasta structures dissolve? Up to which temperatures is the ansatz of a Wigner Seitz cell valid? We have tried to validate a simple coexistence phase approach to obtain the pasta phase and its structure by using the results of possible surface energy parametrizations and comparing the final results with the more realistic and self-consistent Thomas-Fermi approximation, which is very time consuming. It remains to be checked how the Thomas-Fermi calculation of β -equilibrium pasta phase compares with the results obtained within Hartree-Fock and Hartree-Fock-Bogoliubov, where only

spherical clusters are considered. More calculations in this direction are still required.

So far, we have included α particles as part of the pasta phase. Will light clusters other than α particles contribute in a significative manner to the extension of the pasta phase and its transition density to homogeneous matter? Moreover, how will the presence of light clusters affect the properties of the pasta phase? Are the values for the dissolution density of the different light clusters in nuclear matter realistic [47]?

We have also seen that the inclusion of the pasta phase affects the neutrino opacities through its diffusion coefficients. It remains to be checked how the internal structure of the pasta phase, which is model and approximation dependent, influences the diffusion coefficients through the different neutrino mean free paths. A more complete calculation will show us how the existence of the pasta structures affect the transport properties of the crust.

Our last section was devoted to a subject other than the crust of neutron stars. The measurement of a pulsar of inferred mass $1.97 \pm 0.04 M_{\odot}$ known as PSR J1614-2230 [48], opened new questions about its possible constituents and related equation of state. It is well known that there is a maximum mass that can be supported against collapse and its theoretical value is very model dependent. According to [49], the maximum mass of a quark star lies between 2 and $2.7 M_{\odot}$. Hence, it is claimed that PSR J1614-2230 can be a quark star. Do quark stars really exist? How are they affected by strong magnetic fields? We have seen that our results for the NJL model cannot reproduce such high masses, not even with very strong magnetic fields.

Acknowledgments - This work was partially supported by the Capes/FCT n. 232/09 bilateral collaboration, by CNPq and FAPESC (Brazil), by FCT and COMPETE/FEDER (Portugal) and by Compstar, an ESF Research Networking Programme. We thank Drs. M. Benghi, M.M. W. de Moraes, J. R. Marinelli, C.C. Barros, L. Brito, S. Chiacchiera, A.M.S. Santos, I. Vidaña, C. Ducoin, Ph. Chomaz, D.B. Melrose, A.P. Martinez and A. Rabhi for our long term collaborations on some of the topics discussed in this chapter.

References

- [1] N. K. Glendenning, *Compact Stars*, Springer-Verlag, New-York, 2000.

-
- [2] N. Itoh, *Prog. Theor. Phys.* 44, 291 (**1970**); A.R. Bodmer, *Phys. Rev. D* 4, 1601 (**1971**); E. Witten, *Phys. Rev. D* 30, 272 (**1984**).
 - [3] C. Alcock, E. Farhi and A. Olinto, *Astrophys. J.* 310, 261 (**1986**).
 - [4] S. Typel and H. H. Wolter, *Nucl. Phys. A* 656, 331 (**1999**); Guo Hua, Liu Bo and M. Di Toro, *Phys. Rev. C* 62, 035203(**2000**).
 - [5] P. Haensel, Final Stages of Stellar Evolution, ed. J.-M. Hameury and C. Motch, (EDP Sciences, 2003), EAS Publ.Ser. 7 (2003) 249.
 - [6] T. Gaitanos, M. Di Toro, S. Typel, V. Baran, C. Fuchs, V. Greco and H. H. Wolter, *Nucl. Phys. A* 732, 24 (**2004**).
 - [7] S.S. Avancini, L. Brito, D. P. Menezes and C. Providência, *Phys. Rev. C* 70, 015203 (**2004**).
 - [8] G. A. Lalazissis, J. König and P. Ring, *Phys. Rev. C* 55, 540 (**1997**).
 - [9] C. J. Pethick and D. G. Ravenhall, *Annu. Rev. Nucl. Part. Sci.* 45, 429 (**1995**). *Phys. A* 584, 675 (**1995**).
 - [10] B. Link, R.I. Epstein, J.M. Lattimer, *Phys. Rev. Lett.* 83 (**1999**) 3362.
 - [11] H. Müller and B. D. Serot, *Phys. Rev. C* 52, 2072 (**1995**).
 - [12] S. S. Avancini, L. Brito, Ph. Chomaz, D. P. Menezes, and C. Providência, *Phys. Rev. C* 74, 024317 (**2006**).
 - [13] C. J. Pethick, D. G. Ravenhall, and C. P. Lorenz, *Nucl. Phys. A* 584, 675 (**1995**).
 - [14] C. Providência, L. Brito, S. S. Avancini, D. P. Menezes, and Ph. Chomaz, *Phys. Rev. C* 73, 025805 (**2006**); L. Brito, C. Providência, A. M. Santos, S. S. Avancini, D. P. Menezes, and Ph. Chomaz, *Phys. Rev. C* 74, 045801 (**2006**).
 - [15] S.S. Avancini, S. Chiacchiera, D.P. Menezes and C. Providência, arXiv:1010.3644v3[nucl-th], *Phys. Rev. C* (**2012**), in press.
 - [16] S.S. Avancini, S. Chiacchiera, D.P. Menezes and C. Providência, *Phys. Rev. C* 82, 055807 (**2010**).

- [17] S.S. Avancini, C.C. Barros, D.P. Menezes and C. Providência, *Phys. Rev. C* 82, 025808 (2010).
- [18] H. Sonoda, G. Watanabe, K. Sato, K. Yasuoka, and T. Ebisuzaki, *Phys. Rev. C* 77, 035806 (2008); *ibid*, *Phys. Rev. C* 81, 049902 (2010).
- [19] W. G. Newton and J. R. Stone, *Phys. Rev. C* 79, 055801 (2009).
- [20] S. Typel, G. Roepke, T. Klahn, D. Blaschke and H.H. Wolter, *Phys. Rev. C* 81, 015803 (2010).
- [21] B. A. Li, L. W. Chen and C. M. Ko, *Phys. Rep.* 464, 113 (2008).
- [22] U. Garg *et al.*, *Nucl. Phys. A* 788, 36 (2007).
- [23] P. Danielewicz and J. Lee, *Nucl. Phys. A* 818, 36 (2009).
- [24] B. A. Li, G.-C. Yang and W. Zuo, *Phys. Rev. C* 71, 014608 (2005).
- [25] C. Fuchs, *Prog. Part. Nucl. Phys.* 56, 1 (2006).
- [26] D.V. Shetty, S.J. Yennello, *Pramana*, 75 (2010) 259; arXiv:1002.0313v4 [nucl-ex].
- [27] B. A. Brown, *Phys. Rev. Lett.* 85, 5296 (2000).
- [28] S. Typel and B. A. Brown, *Phys. Rev. C* 64, 027302 (2001).
- [29] C. J. Horowitz and J. Piekarewicz, *Phys. Rev. Lett.* 86, 5647 (2001).
- [30] C. J. Horowitz, S. J. Pollock, P. A. Souder and R. Michaels, *Phys. Rev. C* 63, 025501 (2001).
- [31] B. A. Brown, G. Shen, G. C. Hillhouse, J. Meng and A. Trzcinska, *Phys. Rev. C* 76, 034305 (2007).
- [32] M. Centelles, X. Roca-Maza, X. Viñas and M. Warda, *Phys. Rev. Lett.* 102, 122502 (2009).
- [33] I. Vidaña, C. Providência, A. Polls, and A. Rios, *Phys. Rev. C* 80, 045806 (2009)
- [34] C. Ducoin, J. Margueron, and C. Providência, *Europhys. Lett.* 91, 32001 (2010).

-
- [35] J.A. Pons, A.W. Steiner, M. Prakash and J.M. Lattimer, *Phys. Rev. Lett.* 86 (2001) 5223-5226; J.A. Pons, S. Reddy, M. Prakash, J.M. Lattimer and J.A. Miralles, *Astrophys. J.* 513, 780 (1999); S. Reddy, M. Prakash and J.M. Lattimer, *Phys. Rev. D* 58, 013009 (1998).
- [36] Burrows, A. and Lattimer, J. M., *Apj*, 307, 178,(1986).
- [37] M.D. Alloy and D.P. Menezes, *Phys. Rev. C* 83, 035803 (2011).
- [38] R. Duncan and C. Thompson, *Astron. J* 32, L9 (1992); astro-ph/0002442.
- [39] C. Kouveliotou et al, *Nature* 393, 235 (1998).
- [40] V.V. Usov, *ApJ* 481, L107 (1997).
- [41] C. Kettner, F. Weber, M.K. Weigel, N.K. Gledenning, *Phys. Rev. D* 51, 1440 (1995).
- [42] D.B. Melrose, R. Fock and D.P. Menezes, *Month. Not. Roy. Astr. Soc.* 371, 204 (2006).
- [43] Y. Nambu and G. Jona-Lasinio, *Phys. Rev.* 122, 345 (1961); 124, 246 (1961).
- [44] D.P. Menezes, M. Benghi Pinto, S.S. Avancini and C. Providência, *Phys. Rev. C* 80, 065805 (2009).
- [45] Tolman, R.C., *Phys. Rev.* 55 (1939) 364; J.R. Oppenheimer and G.M. Volkoff, *Phys. Rev.* 55 (1939) 374.
- [46] S.S.Avancini, D.P. Menezes and C. Providência, *Phys. Rev. C* 83, 065805 (2011) .
- [47] S.S. Avancini, C.C. Barros, L. Brito, S. Chiacchiera, D.P. Menezes and C. Providência, *Phys. Rev. C* 85, 035806 (2012).
- [48] F. Ozel, D. Psaltis, S. Ransom, P. Demorest and M. Alford, *ApJ* 724, L199 (2010).
- [49] A. Kurkela, P. Romatschke and A. Vuorinen, *Phys. Rev. D* 81, 105021 (2010).